

CONSTRAINTS ON THE INTRACLUSTER DUST EMISSION IN THE COMA CLUSTER OF GALAXIES

TETSU KITAYAMA¹, YUICHI ITO¹, YOKO OKADA^{2,8}, HIDEHIRO KANEDA^{2,3}, HIDENORI TAKAHASHI⁴, NAOMI OTA^{2,5}, TAKASHI ONAKA⁶, YUKA Y. TAJIRI^{6,7}, HIROHISA NAGATA² AND KENKICHI YAMADA¹

ABSTRACT

We have undertaken a search for the infrared emission from the intracluster dust in the Coma cluster of galaxies by the Multiband Imaging Photometer for *Spitzer*. Our observations yield the deepest mid and far-infrared images of a galaxy cluster ever achieved. In each of the three bands, we have not detected a signature of the central excess component in contrast to the previous report on the detection by *Infrared Space Observatory (ISO)*. We still find that the brightness ratio between 70 μ m and 160 μ m shows a marginal sign of the central excess, in qualitative agreement with the *ISO* result. Our analysis suggests that the excess ratio is more likely due to faint infrared sources lying on fluctuating cirrus foreground. Our observations yield the 2σ upper limits on the excess emission within 100 kpc of the cluster center as 5×10^{-3} MJy/sr, 6×10^{-2} MJy/sr, and 7×10^{-2} MJy/sr, at 24, 70, and 160 μ m, respectively. These values are in agreement with those found in other galaxy clusters and suggest that dust is deficient near the cluster center by more than 3 orders of magnitude compared to the interstellar medium.

Subject headings: galaxies: clusters: general – galaxies: clusters: individual (Abell 1656) – infrared: general – intergalactic medium

1. INTRODUCTION

The presence of dust grains in the diffuse intergalactic medium is still an open question. If they exist, they should have great impacts not only on our understanding of galaxy evolution but also on interpretation of high-redshift observational data. From X-ray measurements of heavy metal lines, it is evident that clusters and groups of galaxies contain a significant amount of elements processed in galaxies (e.g., Tamura et al. 2004, and references therein). Such elements are likely to have been expelled out of galaxies through ram pressure stripping, galaxy mergers and interactions, blowout by supernovae, etc. Dust may also be expelled by these processes or by some independent mechanism such as radiation pressure (e.g., Chiao & Wickramasinghe 1972; Ferrara et al. 1991). The X-ray emitting hot gas can collisionally heat the dust (Dwek 1986), while it can also destroy small dust grains via sputtering (Draine & Salpeter 1979; Tsai & Mathews 1995). Dust grains coexistent with the X-ray emitting gas have indeed been detected in a number of elliptical galaxies (e.g., Knapp et al. 1989; Kaneda et al. 2007; Temi et al. 2007). The temperature, the amount, and the size distribution of the dust in hot plasma can be quite different from those in the normal

interstellar medium (see Dwek & Arendt 1992 for review on dust-gas interactions). Once detected firmly, the intracluster or intragroup dust will definitely provide a powerful probe of galaxy evolution and the dust-gas interaction.

There have been several suggestions and debates regarding the presence of dust in clusters and groups of galaxies. Over five decades ago, Zwicky (1957) first suggested an enhanced extinction toward the Coma cluster of galaxies. More recently, Girardi et al. (1992) pointed out that the redshift asymmetries of member galaxies in nearby groups are consistent with the presence of dust in the intragroup medium. The observed oxygen K edge in an X-ray spectrum of the Perseus cluster can also be attributed to intracluster dust grains (Arnaud & Mushotzky 1998). The extended submillimeter emission detected in a rich galaxy cluster may partly be due to dust (Komatsu et al. 1999; Kitayama et al. 2004). There have been extensive searches for the enhanced visual extinction toward high redshift objects behind clusters (Maoz 1995; Nollenberg et al. 2003; Muller et al. 2008) and Chelouche et al. (2007) reported the detection of reddening toward $z \sim 0.2$ clusters. On the other hand, the intracluster dust is likely to enhance the efficiency of gas cooling (Dwek 1987) that is in apparent contradiction with recent X-ray observations (Peterson et al. 2003).

More direct evidence has been searched for in the far-infrared bands. Hickson et al. (1989) reported that the far-infrared emission observed with *IRAS* is enhanced by about a factor of 2 in compact groups of galaxies compared with a sample of isolated galaxies. The extended excess emission is also inferred toward Abell 262 and Abell 2670 (Wise et al. 1993). Sulentic & De Mello Rabaca (1993), however, pointed out that the results of Hickson et al. (1989) are likely to have been overestimated mainly due to the limited spatial resolution of *IRAS*. Stickel et al. (1998) and Stickel et al. (2002) reported the detection of ex-

¹ Department of Physics, Toho University, Funabashi, Chiba 274-8510, Japan

² Institute of Space and Astronautical Science, Japan Aerospace Exploration Agency, 3-1-1 Yoshinodai, Sagami-hara, Kanagawa 229-8510, Japan

³ Division of Particle and Astrophysical Sciences, Nagoya University, Chikusa-ku, Nagoya 464-8602, Japan

⁴ Gunma Astronomical Observatory, 6860-86 Nakayama, Takayama-mura, Agatsuma-gun, Gunma 377-0702, Japan

⁵ Max-Planck-Institut für extraterrestrische Physik, 85748 Garching, Germany

⁶ Department of Astronomy, The University of Tokyo, Tokyo 113-0033, Japan

⁷ Nippon System Development Co. Ltd., Tokyo, Japan

⁸ Present address: I. Physikalisches Institut, Universität zu Köln, Zùlpicher Str. 77, 50937 Köln, Germany

tended excess far-infrared emission from the Coma cluster, which can be attributed to thermal emission from the intracluster dust. They find such emission only in one out of six clusters they observed with *Infrared Space Observatory (ISO)*. Montier & Giard (2005) combined the *IRAS* maps toward 11,507 galaxy clusters and statistically detected the excess emission, although the contribution of member galaxies is yet to be fully removed.

Major difficulties in the previous infrared searches are the limited sensitivity and spatial resolution of the detectors. These limitations may have led to significant contamination of individual galaxies as well as Galactic cirrus confusion. It will therefore be meaningful to perform infrared observations using current facilities with much improved sensitivity and spatial resolution. Bai et al. (2007) searched for the intracluster dust emission from Abell 2029 with *Spitzer* and reported that the cirrus noise limits the detection of the intracluster dust component.

In this paper, we present the results of our deep observations toward the central region of the Coma cluster (Abell 1656) with the Multiband Imaging Photometer for *Spitzer* (MIPS) on board the *Spitzer* Space Telescope. Coma lies at high galactic latitude ($b = 88^\circ$) where the cirrus level is expected to be among the lowest. In fact, Stickel et al. (1998) and Stickel et al. (2002) found with *ISO* the excess far-infrared emission toward Coma based on the brightness ratio $I_{120\mu\text{m}}/I_{180\mu\text{m}}$, while the S/N at each wavelength is still insufficient to detect the excess directly and the contamination of galaxies is not removed. We attempt to probe the excess emission more directly by approaching the confusion limits of extragalactic sources and Galactic cirrus in each band.

Throughout the paper, we assume a standard set of cosmological parameters, $\Omega_m = 0.27$, $\Omega_\Lambda = 0.73$, and $h = 0.71$ consistent with the *WMAP* five year data (Komatsu et al. 2009). An angular size of $1''$ corresponds to a physical size of 0.46 kpc at the redshift $z = 0.0231$ of the Coma cluster.

2. OBSERVATIONS AND DATA REDUCTION

The central region of the Coma cluster was observed at 24, 70 and 160 μm with the MIPS in our GO3 program on 2007 January 19. Total duration of the observation was 41 ksec. Linear scans were performed in a slow scan mode covering the $5' \times 50'$ region across the cluster as shown in Figure 1 (the scan width was reduced to $\sim 2.5'$ at 70 μm due to dead pixels). The scan paths were carefully chosen so as to avoid bright galaxies and to lie close to the cluster center; the scan center was fixed at the mid-point ($12^{\text{h}}59^{\text{m}}51.9^{\text{s}}$, $+27^\circ58'05''$) between two massive central galaxies, NGC4874 and NGC4889 with the position angles of -25.4° , -28.9° and -25.2° at 24, 70 and 160 μm , respectively. The above scan center is $3.2'$ northeast of the X-ray center of the cluster in the *ROSAT* PSPC image ($12^{\text{h}}59^{\text{m}}40.1^{\text{s}}$, $+27^\circ56'56''$). This separation is small compared to the extent of the X-ray emission, which is characterized by the core radius of $10'$. In total, 32 scans were performed in each band, 16 of which repeatedly covered a $5' \times 30'$ region on either side of the scan center. The integration time per pixel after 16 scans was 1600, 1600 and 160 sec at 24, 70 and 160 μm , respectively. Two sets of the 16 scan legs overlapped and the integration time was doubled in the central $5' \times 10'$ region, where the X-ray emission is the most prominent.

The data were first processed with the MIPS pipeline, version S17 (Gordon et al. 2005) to yield the Basic Calibrated Data (BCD). To further improve the images, the pixel-dependent and scan-dependent backgrounds were corrected as follows. In doing so, special care was taken to maintain the extended nonlinear component of the emission. All the results regarding the extended emission are based on unfiltered images.

First, we create a median flat field of detector pixels by stacking the normalized BCD frames, excluding the regions within $10'$ from the cluster center. The normalization is done by dividing each BCD by its median. This is intended to separate any large-scale variations, e.g., due to the zodiacal light, from the pixel-dependent backgrounds and applied solely to create the flat field. We have checked that the flat field so obtained is properly normalized; its mean is equal to unity within 0.2%. We then divide the original BCD (not normalized) by the normalized median flat field. At 24 μm , we further remove scattered light that produces a background modulation as a function of the scan mirror position; the average offset at each scan mirror position is computed excluding the data within $10'$ from the cluster center. As mentioned below, these processes will be re-run after the source identification.

Second, we create for each band a mosaic image using the MOPEX software package, version 18.2 (Makovoz & Khan 2005) developed at the Spitzer Science Center. The pixel size is taken to be a nominal value of $2.45''$, $4.0''$ and $8.0''$ at 24, 70 and 160 μm , respectively. We exclude the first five BCD frames in each scan leg to omit boost frame transients. We also exclude the frames affected by stimulator flashes at 70 and 160 μm . The background matching is applied *after* combining the frames in each scan leg; we only correct the constant offsets among 32 scan legs to assure sufficiently large overlapping area and to preserve any extended feature of the emission.

Third, we identify point sources in the mosaic images down to the 1σ detection limit (~ 0.02 , ~ 2 and ~ 20 mJy at 24, 70 and 160 μm , respectively) using APEX (Makovoz & Marleau 2005). This limit corresponds to the $2 \sim 3\sigma$ confusion level in each band (Dole et al. 2004b). The regions around the sources are masked out and unused in our analysis. More specifically, the source identification and the masking procedure are done on the basis of median-subtracted images; a median-filtered image is created and subtracted from the unfiltered image solely for this purpose. To improve the efficiency of source detection against unknown background fluctuations, we vary the size of a median filter box from 5×5 to 25×25 pixels. For every source identified in each median-subtracted image, we estimate the radius r_{mask} at which the surface brightness, including that of the side-lobes, drops below a certain threshold noise level using the Point Response Function. We adopt 0.5σ as the threshold noise level at 24 and 70 μm , and 1σ at 160 μm , considering the lower uniformity of the data in the latter band. We then return to the *unfiltered* image and mask all the pixels within r_{mask} from the sources identified in any of the median-subtracted images. We have checked that the correlation coefficient between the mean brightness of masked pixels ($r < r_{\text{mask}}$) and that of unmasked pixels at $r_{\text{mask}} < r < 2r_{\text{mask}}$ is less than 0.2 in any of

the median-subtracted images. We thus consider that our masking procedure successfully removes the contribution of resolved sources.

Strictly speaking, the source identification and the background correction are not independent of each other. We therefore repeat the above procedure from the flat-field correction excluding the pixels around the point sources in the BCD.

After applying the above corrections, we subtract from each unfiltered image the linear gradient over the entire map, so as to remove the variation on scales larger than the galaxy cluster. Such a gradient is greatest at $24\ \mu\text{m}$ due to the zodiacal light; it causes the difference of $\Delta I_\nu > 1\ \text{MJy/sr}$ between the map edges which is more than 2 orders of magnitude larger than the average noise level of the image (Table 1). By simply subtracting the linear component, we avoid relying on specific models of the zodiacal light emission that are still uncertain at scales probed here. To preserve the average brightness of the entire map, the brightness at the scan center is kept unchanged by the subtraction.

3. RESULTS

Figure 2 shows the mosaic images after the subtraction of the linear gradient. The point sources are explicitly shown for display purposes. The pixel sizes of the images, the FWHMs of the Point Response Function, and the average noise levels are listed in Table 1. We have assigned a noise to an individual pixel as the larger of the uncertainty estimated in the MIPS pipeline and the standard deviation of actual measurements at that pixel. The latter is on average twice as large as the former at 70 and $160\ \mu\text{m}$, and both are comparable at $24\ \mu\text{m}$. This choice should enable us to take account of any residual systematics in each pixel more properly. Note that the sensitivity at $160\ \mu\text{m}$ is likely limited by Galactic cirrus; the 1σ fluctuation level expected at the position of Coma is $5.4 \times 10^{-3}\ \text{MJy/sr}$ at $70\ \mu\text{m}$ and $0.20\ \text{MJy/sr}$ at $160\ \mu\text{m}$ (Jeong et al. 2005).

Masking the regions around the detected sources removes 38%, 66% and 64% of the pixels in the 24, 70 and $160\ \mu\text{m}$ images, respectively. We plot the histograms of the pixels with and without masking in Figure 3. In all bands, the histograms before masking are positively skewed due to bright sources. Once the sources are excluded, the data follow the Gaussian distribution more closely, while there are small excesses at high σ . These excesses are due to low-significance data affected by noisy detector arrays or low coverage. Since the noise assigned to such data is large, their contribution to the mean brightness is negligible. At $160\ \mu\text{m}$, the 1σ range of the distribution after the source mask, $0.19\ \text{MJy/sr}$, is likely affected by the fluctuations of Galactic cirrus emission (Jeong et al. 2005). At 24 and $70\ \mu\text{m}$, the 1σ ranges, 0.011 and $0.11\ \text{MJy}$, are comparable to the average noise level listed in Table 1.

Figures 4–6 show the surface brightness distribution along the scan path as a function of the distance from the X-ray center of the cluster (negative values of the distance are assigned to the pixels at lower declination than the X-ray center). We plot the brightness at each pixel and their binned average. Unless otherwise stated, the error bar indicates the 1σ statistical error of the mean in each bin. The $70\ \mu\text{m}$ data are lacking within $1.7'$ from

the X-ray center due to dead pixels. We hence adopt fiducially the bin size of $3.6'$ ($100\ \text{kpc}$) in the present paper so that it fully covers the deficit region while it is still sufficiently smaller than the X-ray core radius of $10'$. In all bands, the fluctuations in the brightness, particularly the spikes due to point sources, are significantly reduced after the source mask, yet there is no indication of the central excess.

In the bottom panels of Figures 4–6, we plot the mean brightness of the removed component, i.e., the difference between the unmasked and masked brightness. From our linear scans within $\sim 30'$ from the cluster center, we do not find a central concentration of the integrated source intensities either. The average levels of the removed brightness are $0.012\ \text{MJy/sr}$, $0.093\ \text{MJy/sr}$ and $0.16\ \text{MJy/sr}$ at 24, 70 and $160\ \mu\text{m}$, respectively.

We further combine the brightness in the two directions from the cluster center and compare its radial profile with model predictions in Figure 7. The prediction for the intracluster dust emission is based on the theoretical model of Yamada & Kitayama (2005) (see the next section for details). For direct comparison with the *ISO* results, we have adjusted the total amount of dust to reproduce the excess brightness of $0.2\ \text{MJy/sr}$ at $120\ \mu\text{m}$ within the radius of $1.5'$ inferred in Stickel et al. (2002). Since we are only interested in the difference of the signal across the cluster, an offset is added to the model brightness to match the mean brightness of the whole map at the edge. At $24\ \mu\text{m}$, the absence of the excess is as expected since the predicted temperature of the intracluster dust is relatively low, $20\text{--}30\text{K}$ (see also Dwek et al. 1990). At 70 and $160\ \mu\text{m}$, the foreground/background fluctuations are comparable to the expected levels of the emission and we do not find a sign of the central excess in either band.

From the observed brightness within $r = 3.6'$ relative to the mean of the entire map, we obtain 2σ upper limits on the central excess as 5.2×10^{-3} , 6.0×10^{-2} and $6.6 \times 10^{-2}\ \text{MJy/sr}$, at 24, 70 and $160\ \mu\text{m}$, respectively. In deriving these limits, we have taken into account the background/foreground fluctuations that dominate over the statistical noise as follows. We have randomly selected a circular region of radius $3.6'$ from the map in each band 100 times. From the variance of the mean brightness of selected regions, we have assigned an 1σ error of 1.9×10^{-3} , 2.1×10^{-2} and $6.6 \times 10^{-2}\ \text{MJy/sr}$ at 24, 70 and $160\ \mu\text{m}$, respectively.

Stickel et al. (1998) and Stickel et al. (2002) found with *ISO* the excess far-infrared emission toward the center of this cluster based on the surface brightness ratio $I_{120\mu\text{m}}/I_{180\mu\text{m}}$. Although the scan paths and the observed bands are not exactly the same in our observations, we attempt to mimic their analysis by presenting $I_{24\mu\text{m}}/I_{70\mu\text{m}}$ and $I_{70\mu\text{m}}/I_{160\mu\text{m}}$ in Figure 8. While the fluctuation is large, there appears to be a weak sign of a central enhancement in $I_{70\mu\text{m}}/I_{160\mu\text{m}}$. The enhancement is largely due to a variation in the $160\ \mu\text{m}$ map around the cluster center (Fig.2); there are bright extended regions at $\sim 10'$ on each side, presumably produced by far-infrared sources lying on fluctuating cirrus foreground. We have checked that no counterparts are detected in the *Chandra* X-ray image of this region. While some of the sources are apparent and removed at $70\ \mu\text{m}$, the lower spatial resolution and the larger cirrus fluctuation prevent us from removing them completely at $160\ \mu\text{m}$.

In turn, the cluster center appears to be darker than its surrounding at $160\ \mu\text{m}$, resulting in the apparent excess in $I_{70\mu\text{m}}/I_{160\mu\text{m}}$. Figure 6 also indicates that the depression at $160\ \mu\text{m}$ is not due to over-removal of the sources at the center. We therefore do not consider this to be a detection of the intracluster dust.

4. DISCUSSION

While there is no direct evidence of the central excess in any of the three bands observed by the MIPS, we still find a weak sign of excess in the brightness ratio $I_{70\mu\text{m}}/I_{160\mu\text{m}}$ that may resemble the excess in $I_{120\mu\text{m}}/I_{180\mu\text{m}}$ reported by Stickel et al. (1998) and Stickel et al. (2002). It is therefore meaningful to explore the consistency of these results.

For this purpose, we subtract from our data the average zodiacal light and the cosmic infrared background levels estimated by the *Spitzer* background estimator (Reach 2000) at the scan center position for the date of observation; $I_{\text{ZOD}} = 7.21$ and 1.41 MJy/sr, $I_{\text{CIB}} = 0.21$ and 1.30 MJy/sr at 70 and $160\ \mu\text{m}$, respectively. We subtract the above values from the whole map since we have already corrected the linear gradient of the map relative to the scan center. We have checked that subtracting position-dependent zodiacal light levels prior to the correction of the linear gradient changes the resulting brightness ratio by no more than 5%. The uncertainties in the absolute calibration are not significant either; 5% at $70\ \mu\text{m}$ and 12% at $160\ \mu\text{m}$ (Gordon et al. 2007; Stansberry et al. 2007). However, simply because the mid-infrared brightness is dominated by the zodiacal light, the nominal error of $\sim 15\%$ in its model (Reach 2000) will change the brightness after subtraction at 70 and $160\ \mu\text{m}$, ~ 1.1 MJy/sr and ~ 1.9 MJy/sr, by $\sim 100\%$ and $\sim 10\%$, respectively. Keeping these large uncertainties in mind, we investigate the origin of the excess in the band ratio as follows.

Figure 9 shows the radial distribution of the brightness ratio $I_{70\mu\text{m}}^{\text{corr}}/I_{160\mu\text{m}}^{\text{corr}}$ after the correction mentioned above. The error bars include only the statistical uncertainties. Assuming that the corrected brightness distribution is produced by a combination of a central excess and more extended component, e.g., Galactic cirrus, we apply equation (7) of Stickel et al. (2002) to our observed bands and obtain $I_{70\mu\text{m}}^{\text{excess}} \sim 6.4 \times 10^{-2}$ MJy/sr within the radius of $3.6'$. This value is comparable to the 2σ upper limit of 6.0×10^{-2} MJy/sr derived solely from the $70\ \mu\text{m}$ data in the previous section. The central excess, if real, should have been nearly canceled at $70\ \mu\text{m}$ by the fluctuation of the other component. The interpretation of the central excess for the origin of the observed $I_{70\mu\text{m}}/I_{160\mu\text{m}}$ profile is therefore rather unlikely, although it is not fully rejected.

Note that equation (7) of Stickel et al. (2002) is based on a key assumption that the excess component contributes only to the variation of the shorter wavelength data. Alternatively, it is also possible to interpret the same data with the variation of the longer wavelength data. In the present observation, a plausible explanation may be that the corrected brightness is still dominated by unresolved sources lying on the fluctuating cirrus foreground, i.e., the absolute values of the signal in both bands are dominated by such sources while the fluctua-

tions at $160\ \mu\text{m}$ are mainly produced by underlying cirrus emission. In fact, the value of $I_{70\mu\text{m}}^{\text{corr}}/I_{160\mu\text{m}}^{\text{corr}} = 0.55 \sim 0.6$ shown in Figure 9 corresponds to the dust temperature of $T_d \sim 25$ K for the absorption efficiency of $Q_{\text{abs}} \propto \lambda^{-2}$ (Draine & Lee 1984). This temperature is higher than the nominal temperature of Galactic cirrus $T_d \sim 18$ K for which the brightness ratio is lower by more than a factor of 5. The mean values of $I_{70\mu\text{m}}^{\text{corr}} \sim 1.1$ MJy/sr and $I_{160\mu\text{m}}^{\text{corr}} \sim 1.9$ MJy/sr are also higher than the levels of the cirrus emission expected for this region, suggesting the contribution of yet unresolved components.

From the limits on the infrared brightness in each band, we further attempt to derive constraints on the amount of the intracluster dust. Model predictions shown in Figure 7 (Yamada & Kitayama 2005) rely on an assumption that the dust is supplied continuously to the intracluster medium from galaxies with the initial size distribution similar to our Galaxy, $dn^{\text{init}}/da \propto a^{-3.5}$ (Mathis et al. 1977), and has reached a steady state against sputtering with the size distribution $dn/da \propto a^{-2.5}$. The galaxy distribution is assumed to trace that of the dark matter given by the Navarro–Frenk–White density profile (Navarro et al. 1997), and the gas density follows the isothermal beta model. Given these, the curves plotted in Figure 7 correspond to the dust surface density of $\Sigma_d = 1.1 \times 10^3$ $\text{M}_{\odot} \text{ kpc}^{-2}$ within the central $3.6'$ of the cluster. The 2σ upper limits on the excess brightness derived in the previous section are 1.3 and 0.37 times the model brightness averaged within the central $3.6'$ at $70\ \mu\text{m}$ and $160\ \mu\text{m}$, respectively. Considering much lower uniformity of the data at $160\ \mu\text{m}$, we take the limit of the $70\ \mu\text{m}$ data to obtain $\Sigma_d < 1.4 \times 10^3$ $\text{M}_{\odot} \text{ kpc}^{-2}$. This limit corresponds to the dust-to-gas-mass ratio of less than 1×10^{-5} within the central 100 kpc, which is nearly 3 orders of magnitude smaller than the Galactic value (Draine 2003).

The average visual extinction A_V is related to the dust surface density as (Spitzer 1978)

$$A_V = 0.011 \left(\frac{Q_{\text{ext}}}{2} \right) \left(\frac{\Sigma_d}{10^3 \text{ M}_{\odot} \text{ kpc}^{-2}} \right) \times \left(\frac{\rho_d}{3 \text{ g cm}^{-3}} \right)^{-1} \left(\frac{a}{0.1 \mu\text{m}} \right)^{-1} \quad (1)$$

where Q_{ext} is the extinction efficiency factor, ρ_d is the dust mass density, and a is the grain radius. Adopting the standard values for Q_{ext} , ρ_d and a quoted in the above equation, our derived limit of $\Sigma_d < 1.4 \times 10^3$ $\text{M}_{\odot} \text{ kpc}^{-2}$ corresponds to $A_V < 0.016$ within the central 100 kpc. On the other hand, Chelouche et al. (2007) report the detection of the mean $E(B - V)$ of a few times 10^{-3} mag toward SDSS QSOs behind $\sim 10^4$ clusters, and Muller et al. (2008) obtain the limit $\langle A_V \rangle < 0.024$ (2σ) from reddening of $\sim 90,000$ background galaxies for 458 clusters. While these optical measurements are given for much larger ($> \text{Mpc}$) scales, our result is still consistent with them.

Finally, gravitational lensing can impact on the emission of background sources behind galaxy clusters. As the total surface brightness is conserved by lensing, the bias in the resolved or unresolved brightness is caused solely by the sources that exceed the detection limit as a result of magnification (Refregier & Loeb 1997). The

number of such sources is $f \equiv \mu^\alpha - 1$ times the number of unlensed sources already lying above the flux limit S , where μ is the magnification and α is the index of the unlensed source count, $N(> S) \propto S^{-\alpha}$. The fractional change in the resolved brightness has the same sign as and is less than f , because the sources contributing to the change have the lowest flux among those resolved. Note that the factor f is different from the bias in the overall surface density given by $\mu^{\alpha-1}$ (e.g., Bartelmann & Schneider 2001). Recent surveys with *Spitzer* yield the mean values of $\alpha = 0.5$ down to $35 \mu\text{Jy}$ at $24 \mu\text{m}$ (Papovich et al. 2004) and $\alpha = 0.6$ down to 1.2 mJy at $70 \mu\text{m}$ (Frayer et al. 2006). The depths of these measurements are comparable to those of the present observation. At $160 \mu\text{m}$, the published counts are currently available for $S > 50 \text{ mJy}$, and an extrapolation using the model of Lagache et al. (2004) yields $\alpha \sim 1.5$ at $S \sim 20 \text{ mJy}$ (Dole et al. 2004a). In the case of Coma, the Einstein radius is $\sim 30''$ and the magnification is expected to vary from $\mu \sim 1.2$ at $r = 3.6'$ to $\mu \sim 1.02$ at $r = 30'$ for a singular isothermal mass profile. Taken together, the above factor in this radius range varies from $f \sim 0.1$ to 0.01 at $24 \mu\text{m}$ and $70 \mu\text{m}$, and $f \sim 0.3$ to 0.03 at $160 \mu\text{m}$. The fractional change in the brightness of the *removed component* shown in Figures 4–6 should therefore be smaller than the variations along the scan path. There is in fact no sign of systematic increase in the resolved brightness toward the cluster center in any band. Owing to the conservation of the total brightness, the bias in the residual unresolved background should also be small. We hence consider that the impact of gravitational lensing is negligible in the present results.

5. CONCLUSIONS

In this paper, we have undertaken a search for the infrared emission from the intracluster dust in the Coma cluster of galaxies by the MIPS on board the *Spitzer* Space Telescope. Our observations yield the deepest mid and far-infrared images of a galaxy cluster ever achieved with average 1σ sensitivities per pixel of $1.3 \times 10^{-2} \text{ MJy/sr}$, $1.1 \times 10^{-1} \text{ MJy/sr}$ and $1.3 \times 10^{-1} \text{ MJy/sr}$ at 24 , 70 and $160 \mu\text{m}$, respectively. In each of the three

bands, we have not detected a signature of the central excess component. Our observations yield the 2σ upper limits on the excess emission within $3.6'$ (100 kpc) of the cluster center as $5.2 \times 10^{-3} \text{ MJy/sr}$, $6.0 \times 10^{-2} \text{ MJy/sr}$, and $6.6 \times 10^{-2} \text{ MJy/sr}$, at 24 , 70 , and $160 \mu\text{m}$, respectively. These results are consistent with the values reported by Bai et al. (2007) for Abell 2029, as well as those derived from a stacking analysis of 11,507 clusters (Montier & Giard 2005).

With the improved spatial resolution and sensitivity of the MIPS, we have obtained much more robust limits on the excess emission from this cluster than previous observations. We still find that the brightness ratio between $70\mu\text{m}$ and $160\mu\text{m}$ shows a marginal sign of the central excess, in qualitative agreement with the finding of Stickel et al. (1998) and Stickel et al. (2002) by *ISO*. Although we cannot fully reject the contribution of the intracluster dust, it is more likely due to unresolved infrared sources lying on fluctuating cirrus foreground.

Combined with the theoretical model of Yamada & Kitayama (2005), we have derived a limit on the surface mass density of the intracluster dust as $\Sigma_d < 1.4 \times 10^3 \text{ M}_\odot \text{ kpc}^{-2}$. This limit corresponds to the dust-to-gas-mass ratio of less than 10^{-5} within the central 100 kpc , which is nearly three orders of magnitude smaller than the Galactic value, implying that the dust destruction is very efficient at the center of the cluster. Our result can further be converted to the limit on the visual extinction of $A_V < 0.02$, which is consistent with the results derived from statistical reddening of background objects behind a large sample of galaxy clusters (Chelouche et al. 2007; Muller et al. 2008).

We thank Takashi Hamana, Nobuhiro Okabe and Norio Sekiya for discussions and an anonymous referee for helpful comments. This work is supported in part by Grant-in-Aid for Young Scientists by MEXT (18740112, 19740112). N.O. acknowledges support from the Alexander von Humboldt Foundation.

REFERENCES

- Arnaud, K. A., & Mushotzky, R. F. 1998, *ApJ*, 501, 119
 Bai, L., Rieke, G. H., & Rieke, M. J. 2007, *ApJL*, 668, L5
 Bartelmann, M., & Schneider, P. 2001, *Physics Reports*, 340, 291
 Chelouche, D., Koester, B. P. & Bowen, D. V. 2007, *ApJ*, 671, L97
 Chiao, R. Y., & Wickramasinghe, N. C. 1972, *MNRAS*, 159, 361
 Dole, H., et al. 2004a, *ApJS*, 154, 87
 Dole, H., et al. 2004b, *ApJS*, 154, 93
 Draine, B. T. 2003, *ARA&A*, 41, 241
 Draine, B.T., & Lee, H. M. 1984, *ApJ*, 285, 89
 Draine, B. T., & Salpeter, E. 1979, *ApJ* 231, 77
 Dwek, E. 1986, *ApJ*, 302, 363
 Dwek, E. 1987, *ApJ*, 322, 812
 Dwek, E., & Arendt, R. G. 1992, *ARA&A* 30, 11
 Dwek, E., Rephaeli, Y., & Mather, J. C. 1990, *ApJ* 350, 104
 Ferrara, A., Ferrini, F., Barsella, B., & Franco, J. 1991, *ApJ*, 381, 137
 Frayer, D. T., et al. 2006, *ApJ*, 647, L9
 Girardi, M., Mezzetti, M., Giuricin, G., & Mardirossian, F. 1992, *ApJ* 394, 442
 Gordon, K. D., et al. 2005, *PASP*, 117, 503
 Gordon, K. D., et al. 2007, *PASP*, 119, 1019
 Hickson, P., Menon, T. K., Palumbo, G. G. C., & Persic, M. 1989, *ApJ* 341, 679
 Jeong, W.-S., Mok Lee, H., Pak, S., Nakagawa, T., Minn K. S., Pearson, C. P., & White, G. J. 2005, *MNRAS*, 357, 535
 Kaneda, H., Onaka, T., Kitayama, T., Okada, Y., & Sakon, I. 2007, *PASJ*, 59, 107
 Kitayama T., Komatsu, E., Ota, N., Kuwabara, T., Suto, Y., Yoshikawa, K., Hattori, M., & Matsuo, H. 2004, *PASJ* 56, 17
 Knapp, G. R., Guhathakurta, P., Dong-Woo, K., & Jura, M. A. 1989, *ApJS*, 70, 329
 Komatsu, E., Kitayama, T., Suto, Y., Hattori, M., Kawabe, R., Matsuo, H., Schindler, S., & Yoshikawa, K. 1999, *ApJ*, L1
 Komatsu, E., et al. 2009, *ApJS*, 180, 330
 Lagache, G., et al. 2004, *ApJS*, 154, 112
 Makovoz, D., & Khan, I. 2005, in *ASP Conf. Ser.* 347, ed. P. Shoppell, M. Britton, & R. Ebert (San Francisco, CA: ASP), 81
 Makovoz, D., & Marleau, F. R. 2005, *PASP*, 117, 1113
 Maoz, D. 1995, *ApJ*, 455, L115
 Mathis J. S., Rumpl W., & Nordsieck K. H. 1977, *ApJ* 217, 425
 Montier, L. A., & Giard, M. 2005, *A&A* 439, 35
 Muller, S., Wu, S.-Y., Hsieh, B.-C., Gonzalez, R. A., Loinard, L., Yee, H. K. C., & Gladders, M. D. 2008, *ApJ*, 680, 975

TABLE 1
PARAMETERS OF THE IMAGES

Wavelength	24 μm	70 μm	160 μm
Pixel size ["]	2.45	4.0	8.0
FWHM ["]	6.2	18	40
Average noise per pixel [MJy/sr]	1.3×10^{-2}	1.1×10^{-1}	1.3×10^{-1}

Navarro, J. F., Frenk, C. S., & White, S. D. M. 1997, ApJ, 490, 493
 Nollenberg, J. G., Williams, L. L. R., & Maddox, S. J. 2003, AJ, 125, 2927
 Papovich, C., et al. 2004, ApJS, 154, 70
 Peterson, J. R., Kahn, S. M., Paerels, F. B. S., Kaastra, J. S., Tamura, T., Bleeker, J. A. M., Ferrigno, C., & Jernigan, J. G. 2003, ApJ 590, 207
 Reach, W. T., 2000, <http://ssc.spitzer.caltech.edu/documents/background/>
 Refregier, A., & Loeb, A. 1997, ApJ, 478, 476
 Spitzer, L. 1978, Physical Processes in the Interstellar Medium (New York: Wiley)
 Stansberry, J.A., et al. 2007, PASP, 119, 1038
 Stickel, M., Klaas, U., Lemke, D. & Mattila, K. 2002, A&A 383, 367

Stickel, M., Lemke, D., Mattila, K., Haikala, L. K. & Haas, M. 1998, A&A 329, 55
 Sulentic, J.W., & De Mello Rabaca, D.F. 1993, ApJ, 410, 520
 Tamura, T., Kaastra, J. S., den Herder, J. W. A., Bleeker, J. A. M., Peterson, J. R. 2004, A&A, 420, 135
 Temi, P., Brighenti, F., & Mathews, W. G. 2007, ApJ, 660, 1215
 Tsai, J. C., & Mathews, W. G. 1995, ApJ, 448, 84
 Wise, M. W., O'Connell, R. W., Bregman, J. N., & Roberts, M. S. 1993, ApJ, 405, 94
 Yamada, K., & Kitayama, T. 2005, PASJ, 57, 611
 Zwicky, F. 1957, Morphological Astronomy (Berlin: Springer)

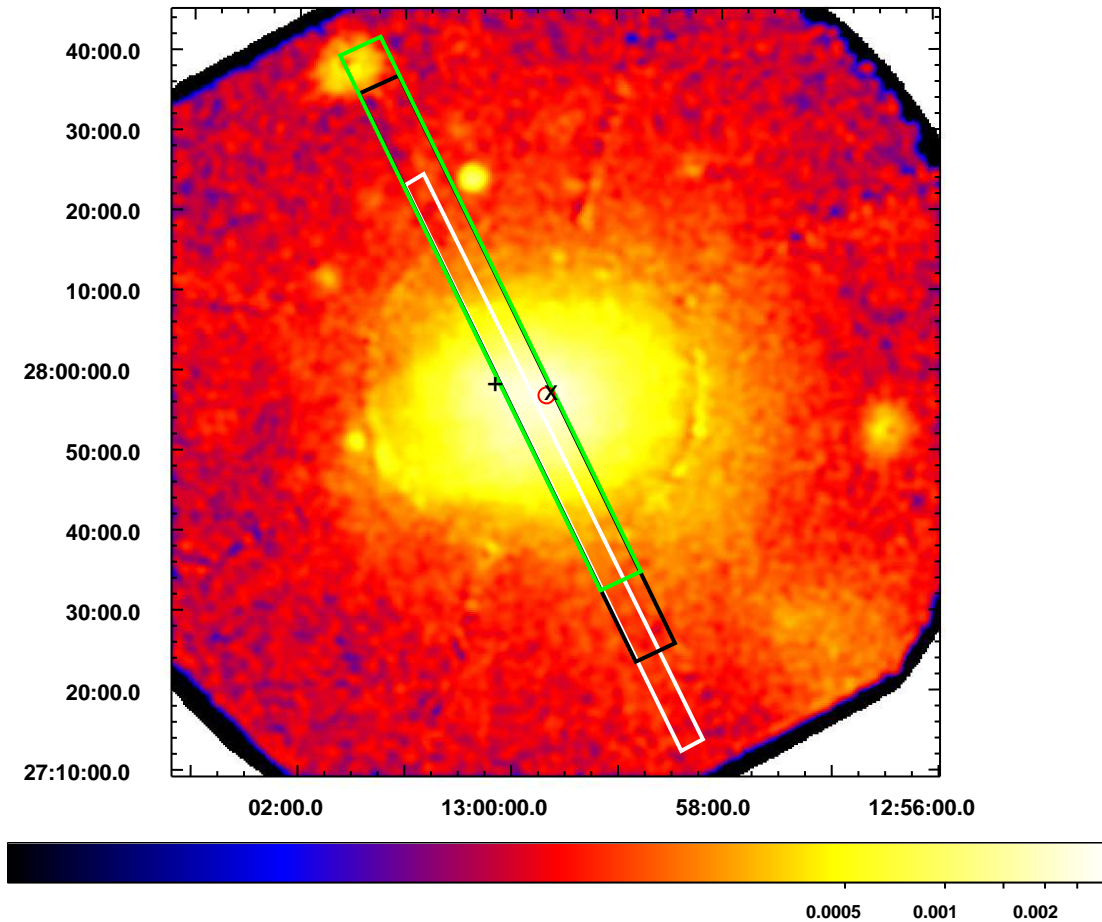


FIG. 1.— Fields-of-view of our *Spitzer*/MIPS observations at 24 μm (black box), 70 μm (white box) and 160 μm (green box) overlaid on the *ROSAT* PSPC X-ray image of the Coma cluster. The X-ray image is scaled logarithmically in units of photons/sec/pixel in the 0.2–2 keV band, after smoothing by a Gaussian filter with $\sigma = 4$ pixel, where the pixel size is 14.9 arcsec. The center of the X-ray surface brightness is indicated by a circle, and the positions of two massive central galaxies, NGC4874 and NGC4889, are marked by a cross and a plus, respectively.

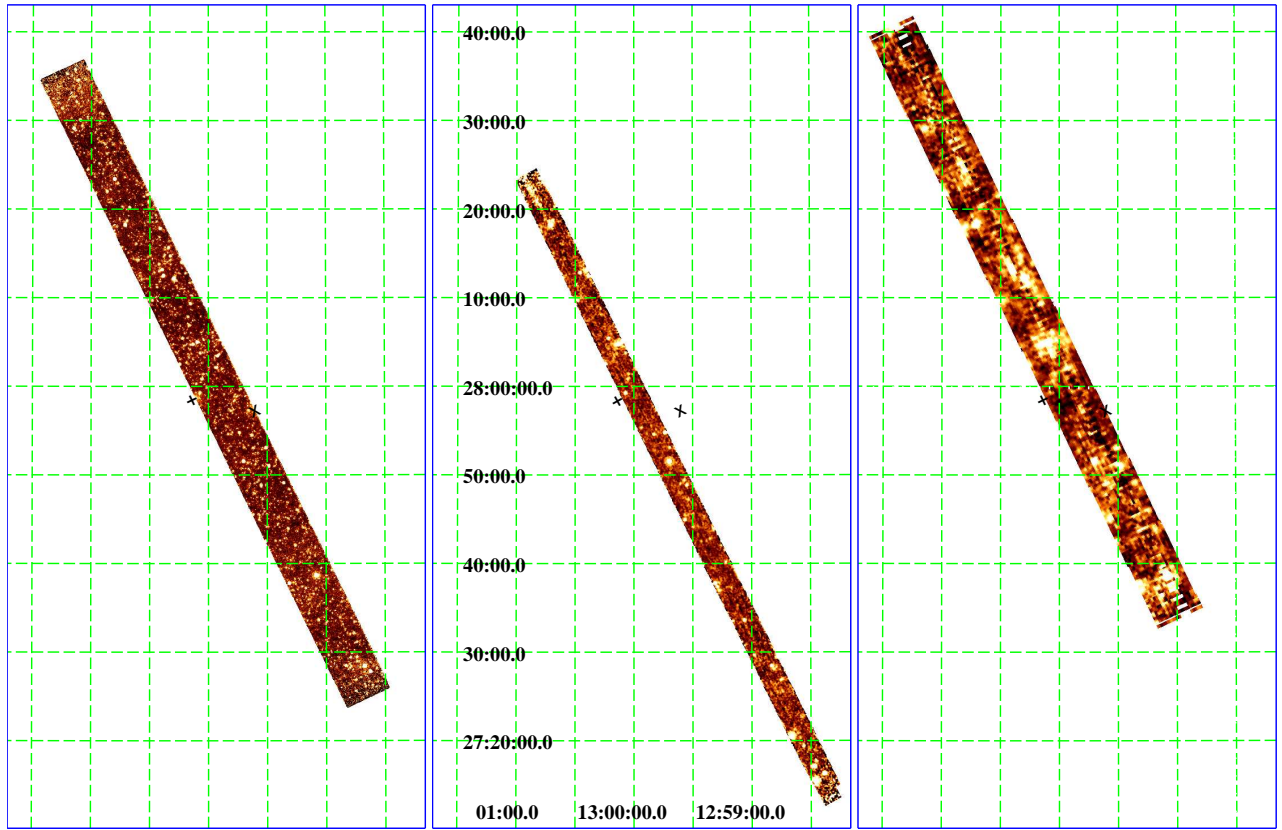


FIG. 2.— Mosaic images at $24\ \mu\text{m}$ (left panel), $70\ \mu\text{m}$ (middle panel), and $160\ \mu\text{m}$ (right panel), respectively. The positions of two massive central galaxies, NGC4874 and NGC4889, are marked by a cross and a plus, respectively.

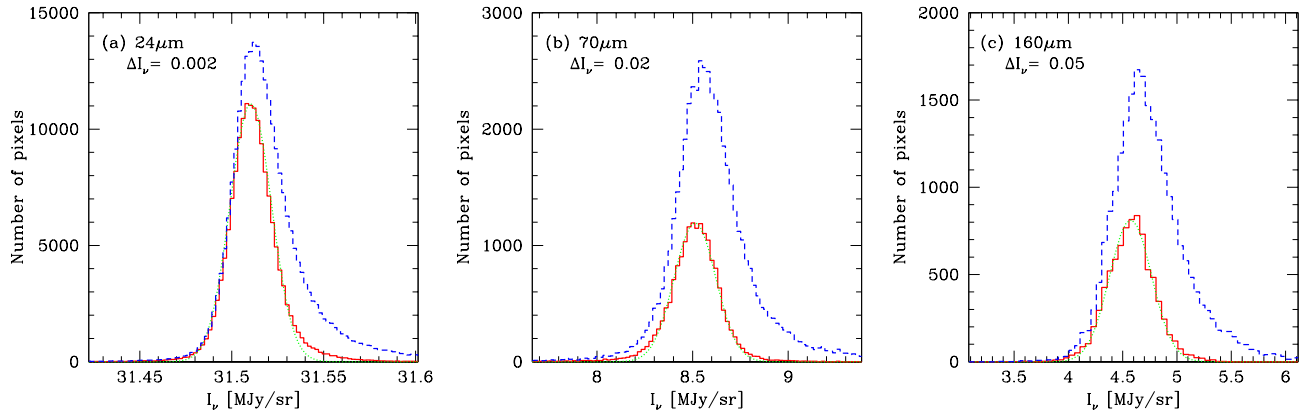


FIG. 3.— Histograms of the image pixels before (dashed curves) and after (solid curves) the source mask at (a) $24\ \mu\text{m}$, (b) $70\ \mu\text{m}$, and (c) $160\ \mu\text{m}$, respectively. Dotted curves indicate, for reference, the Gaussian distribution with $\sigma = 0.011\ \text{MJy/sr}$, $0.11\ \text{MJy/sr}$, and $0.19\ \text{MJy/sr}$ at $24\ \mu\text{m}$, $70\ \mu\text{m}$, and $160\ \mu\text{m}$, respectively.

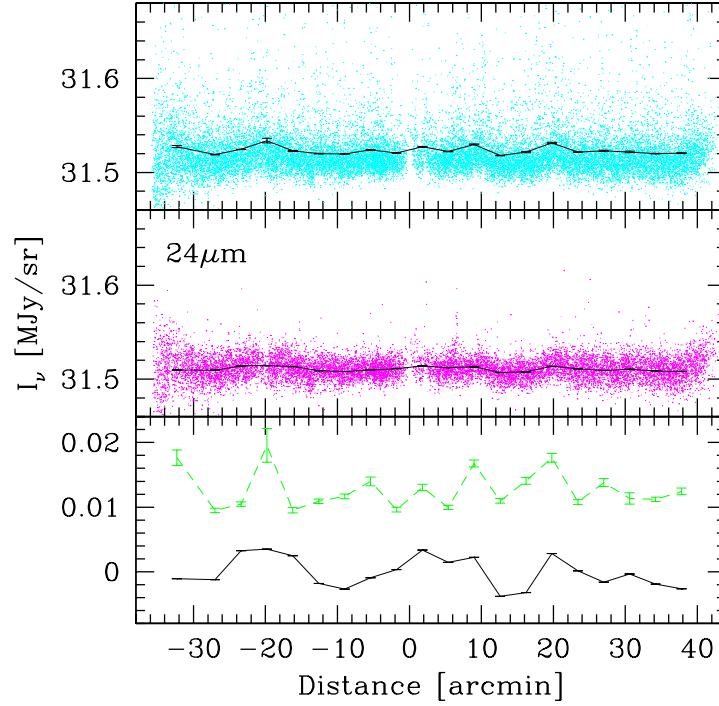


FIG. 4.— *Top*: distribution of the $24\ \mu\text{m}$ brightness along the scan path before the source mask. For clarity, we randomly select and display 1/10 of all the data points. Solid curve indicates the mean brightness with the bin size of $3.6'$ ($100\ \text{kpc}$). *Middle*: same as the top panel except that the surface brightness after the source mask is shown. *Bottom*: dashed curve shows the binned average of the removed component, i.e., the difference between the mean brightness plotted in the top and middle panels. For comparison, solid curve is the same as that in the middle panel except that the average brightness of the whole map is subtracted and the vertical scale is enlarged. In all the panels, the distance is measured from the X-ray center of the cluster with negative values indicating the direction of decreasing declination.

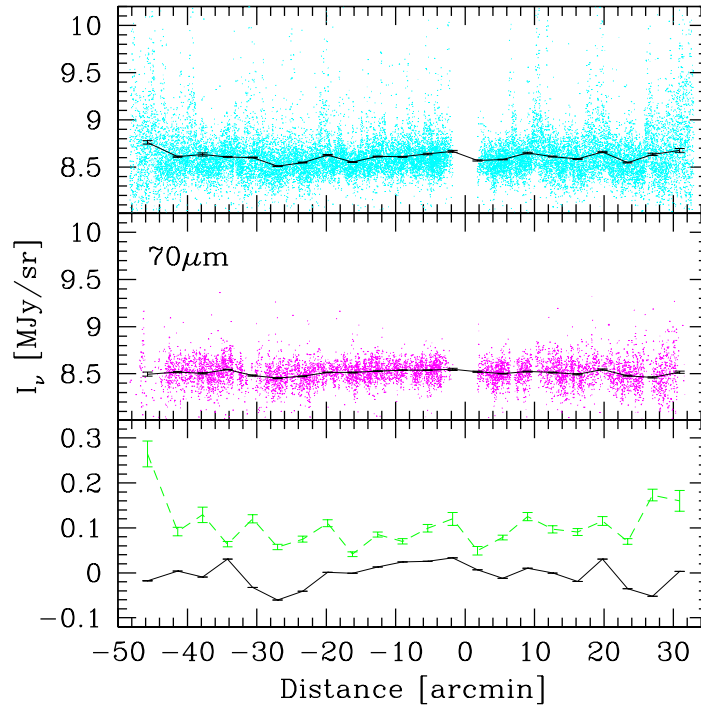


FIG. 5.— Same as Figure 4 except that the $70\ \mu\text{m}$ brightness is shown and, for clarity, 1/2 of all the data points are displayed in the top and middle panels. The $70\ \mu\text{m}$ data are lacking within $1.7'$ from the X-ray center due to dead pixels.

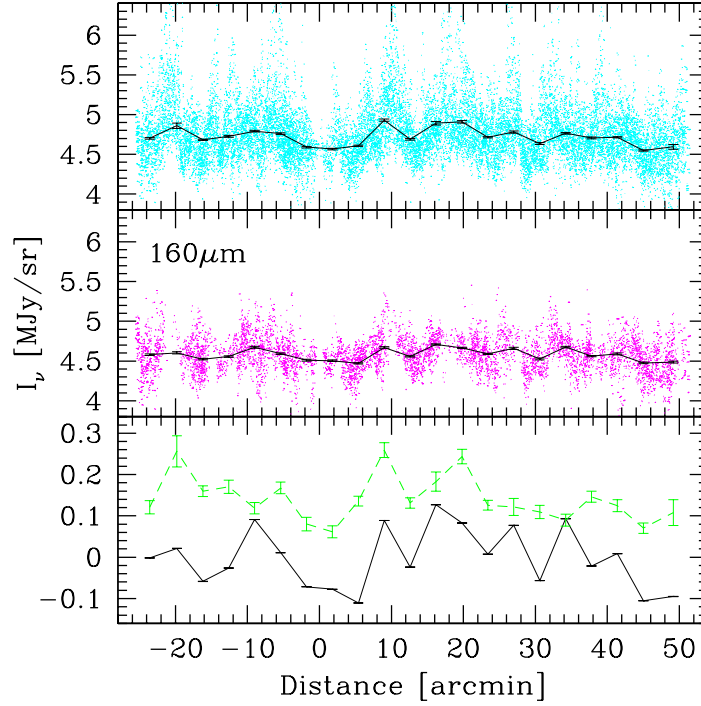


FIG. 6.— Same as Figure 4 except that the $160\ \mu\text{m}$ brightness is shown and all the data points are displayed in the top and middle panels.

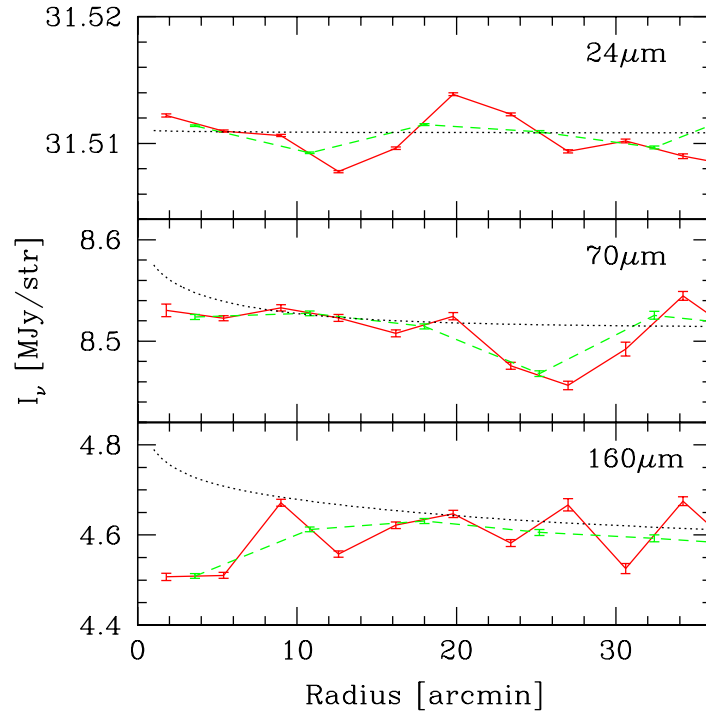


FIG. 7.— Radial profiles of the surface brightness after the source mask at $24\ \mu\text{m}$ (top panel), $70\ \mu\text{m}$ (middle panel), and $160\ \mu\text{m}$ (bottom panel), respectively. Solid and dashed curves indicate the mean brightness with the bin size of $3.6'$ and $7.2'$, respectively. For reference, the prediction for the intracluster emission based the theoretical model of Yamada & Kitayama (2005) is plotted in dotted curves (see the text for details).

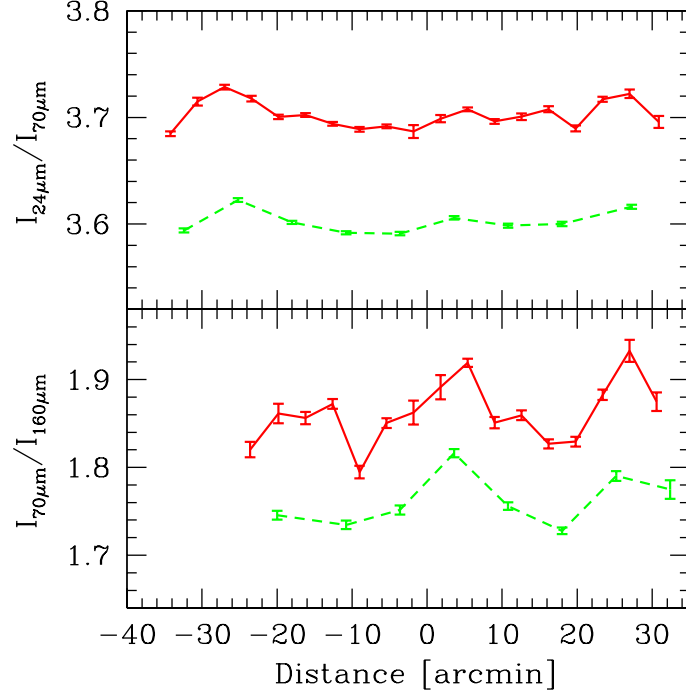


FIG. 8.— Distribution of the brightness ratios $I_{24\mu\text{m}}/I_{70\mu\text{m}}$ (*top panel*) and $I_{70\mu\text{m}}/I_{160\mu\text{m}}$ (*bottom panel*) after the source mask along the scan path. The distance is measured from the X-ray center of the cluster with negative values indicating the direction of decreasing declination. Solid and dashed curves indicate the brightness ratios with the bin size of $3.6'$ and $7.2'$, respectively. For clarity, the dashed curves have been shifted downwards by 0.1 in both panels.

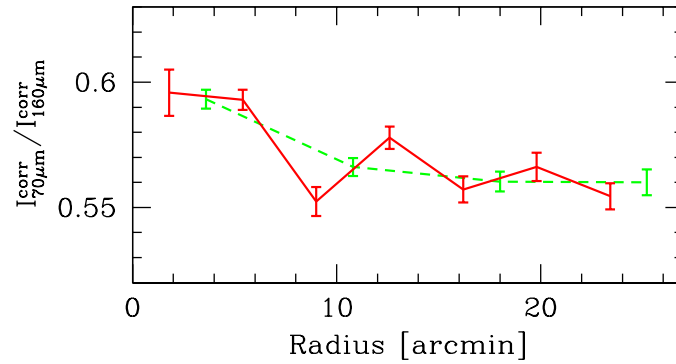


FIG. 9.— Radial profile of the brightness ratio $I_{70\mu\text{m}}^{\text{corr}}/I_{160\mu\text{m}}^{\text{corr}}$ after the source mask and the subtraction of the zodiacal light and the cosmic infrared background. The error bars include only the statistical uncertainties. Solid and dashed curves indicate the brightness ratios with the bin size of $3.6'$ and $7.2'$, respectively.